

Intriguing low-temperature phase in the antiferromagnetic kagome metal FeGe

M. Wenzel,^{1,*} E. Uykur,² A. A. Tsirlin,³ S. Pal,¹ R. Mathew Roy,¹
C. Yi,⁴ C. Shekhar,⁴ C. Felser,⁴ A. V. Pronin,¹ and M. Dressel¹

¹*Physikalisches Institut, Universität Stuttgart, 70569 Stuttgart, Germany*

²*Helmholtz-Zentrum Dresden-Rossendorf, Institute of Ion Beam Physics and Materials Research, 01328 Dresden, Germany*

³*Felix Bloch Institute for Solid-State Physics, Leipzig University, 04103 Leipzig, Germany*

⁴*Max Planck Institute for Chemical Physics of Solids, 01187 Dresden, Germany*

(Dated: January 25, 2024)

The properties of kagome metals are governed by the interdependence of band topology and electronic correlations resulting in remarkably rich phase diagrams. Here, we study the temperature evolution of the bulk electronic structure of the antiferromagnetic kagome metal FeGe using infrared spectroscopy. We uncover drastic changes in the low-energy interband absorption at the 100 K structural phase transition that has been linked to a charge-density-wave (CDW) instability. We explain this effect by the minuscule Fe displacement in the kagome plane, which results in parallel bands in the vicinity of the Fermi level. In contrast to conventional CDW materials, however, the spectral weight shifts to low energies, ruling out the opening of a CDW gap in FeGe.

The kagome lattice has been a fruitful playground to study novel quantum phenomena for over 70 years, uniting electronic correlations, topologically nontrivial states, and geometric frustration [1, 2]. Being rooted in the network of corner-sharing triangles, destructive quantum interference results in localized states, i.e., a flat band over the entire Brillouin zone [3, 4]. Together with the van Hove singularities at the M point, this can lead to exotic electronic orders, including flat-band ferromagnetism, Pomeranchuk instabilities, charge and spin bond order, unconventional superconductivity, nematicity, and Wigner crystallization [5–14].

Several of these intriguing phases have been identified in kagome metals, most prominently the exotic charge-density-wave (CDW) in the superconducting AV_3Sb_5 ($A = K, Rb, Cs$) family [7, 12, 15–18]. Recently, charge order in the context of a magnetic kagome metal has been suggested [19–21]. Hexagonal FeGe crystallizes in the $P6/mmm$ space group featuring magnetic Fe-kagome planes stabilized by Ge1 atoms. Within one unit cell, these kagome layers are separated by a non-magnetic honeycomb lattice of Ge2 atoms as visualized in Fig. 1 (a). At room temperature, an out-of-plane antiferromagnetic (AFM) arrangement of the Fe-kagome layers is found, with ferromagnetically ordered Fe-moments within the kagome planes. This AFM order persists down to approximately 60 K, below which a canted AFM arrangement with an additional reorientation at ~ 30 K is observed [22, 23].

More recent studies reveal an anomaly at $T_C \simeq 100$ K, where a slight drop in the in-plane magnetic susceptibility occurs [19, 24, 25]. However, no clear counterpart to this drop is observed in the electric resistivity [24, 25]. Based on neutron diffraction and scanning tunneling microscopy (STM) measurements, a short-range ordered CDW phase with a minor in-plane lattice distortion on the order of 10^{-4} of the kagome structure has been proposed [19, 21, 24]. Raman spectroscopy and neu-

tron Larmor diffraction further suggested that deviations from the hexagonal symmetry occur above T_C [26].

Although the low-temperature, putative CDW phase of FeGe was investigated extensively by surface-sensitive techniques such as STM and angle-resolved photoemission spectroscopy (ARPES), a systematic study of the temperature-dependent bulk electronic structure remains lacking. Fourier-transform infrared spectroscopy is one of the most effective approaches for investigating bulk CDW order [27–33]. Here, the gap opening at the Fermi level below T_{CDW} is normally manifested in a spectral weight transfer from low to high energies [34]. However, our results on FeGe reveal no indication of a gap opening below the anomaly at T_C and, thus, contradict the CDW scenario at low temperatures. Aided by density functional theory (DFT) calculations of the band structure and the optical conductivity, we show that the reconstruction of the bands due to the structural transition at T_C leads to new interband optical transitions at low energies. We thus interpret the change in the electronic structure below T_C as band splitting rather than gap opening.

High-quality single crystals were synthesized as explained in the Supplemental Material [36]. Prior to the optical experiments, we measured the in-plane magnetic susceptibility and dc resistivity of our samples. The results are plotted in Fig. 1 (b), confirming the stoichiometry and identifying the low-temperature anomaly at $T_C = 102$ K. Fig. 1 (c) displays the temperature-dependent real part of the in-plane optical conductivity. At first glance, the spectra resemble the optical spectra of other magnetic kagome metals such as the ferromagnetic Fe_3Sn_2 [37, 38], and the ferrimagnetic RMn_6Sn_6 compounds [39].

Using the Drude-Lorentz approach, different contributions to the total optical spectra are modeled. In addition to the classical Lorentzian (interband) and Drude (intraband) contributions, a sharp phonon mode around 190 cm^{-1} with a Fano-like shape, and a temperature-

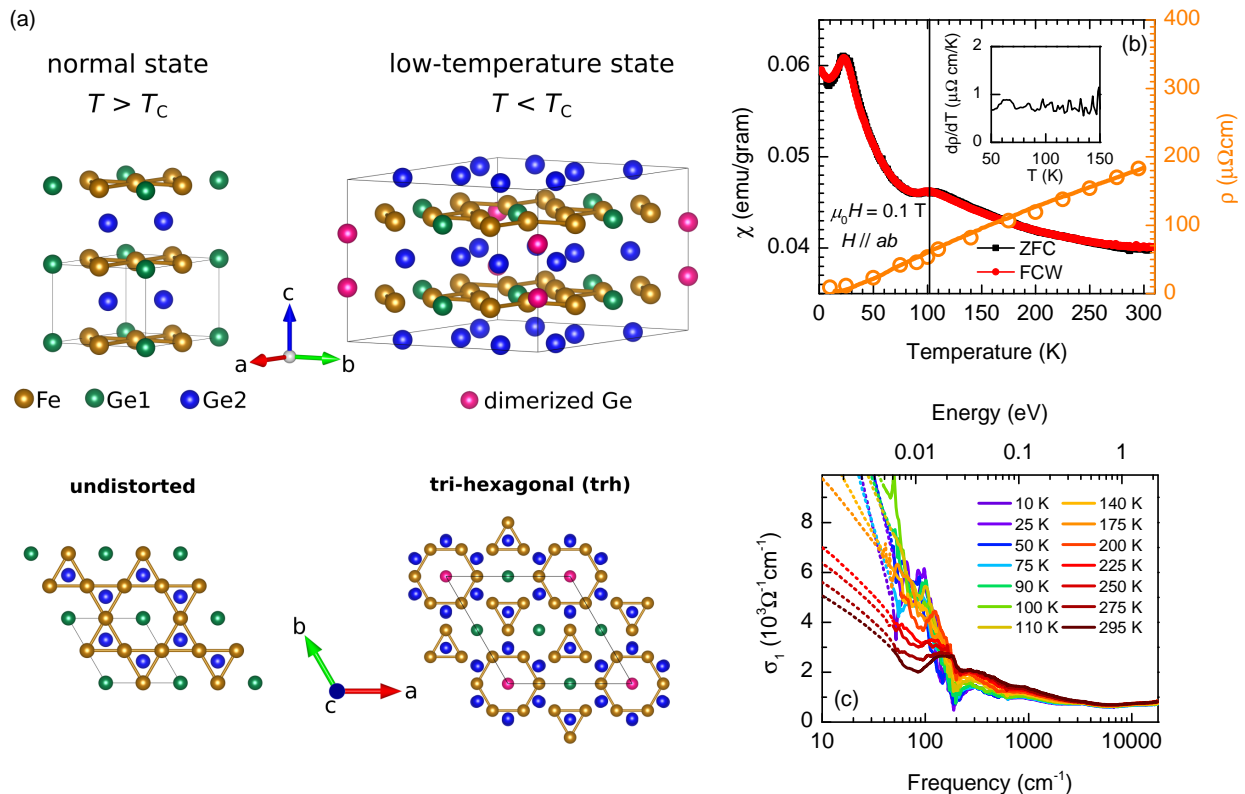


FIG. 1. (a) Crystal structure of hexagonal FeGe in the normal- and the low-temperature state. The bottom panel shows the undistorted in-plane Fe-kagome layer, as well as the tri-hexagonal distortion discussed in the literature [19]. VESTA program was used for the crystal structure visualization [35]. (b) Magnetic susceptibility and electric resistivity curves, measured in the ab -plane. The vertical black line marks the low-temperature anomaly observed in the magnetic susceptibility. Open circles are the dc resistivity values obtained from the Hagen-Rubens fits of the optical measurements as explained in the Supplemental Material [36]. RRR = 51 indicates the good quality of our sample. The inset displays the first derivative of the resistivity. (c) Temperature-dependent in-plane optical conductivity with the dotted lines being the Hagen-Rubens extrapolations to low energies.

dependent absorption peak at low energies are observed. The latter feature is assigned to the intraband signature of localized electrons, in line with previous optical studies of kagome metals [37, 39–43]. The total complex optical conductivity [$\tilde{\sigma} = \sigma_1 + i\sigma_2$] then takes the form

$$\tilde{\sigma}(\omega) = \tilde{\sigma}_{\text{intra}} + \tilde{\sigma}_{\text{phono}} + \tilde{\sigma}_{\text{inter}}. \quad (1)$$

After decomposing the optical data, as shown in Fig. S2 for selected temperatures, it becomes apparent that the low-energy interband transitions strongly vary with temperature. To further visualize these changes, we subtract the Fano resonance and the intraband contributions, i.e., Drude and localization peaks from the optical conductivities as presented in Fig. 2 (a) and (b) for $T > T_C$. The room temperature data is reproduced by our DFT calculations given in panels (c) and (d) via raising the Fermi level by 110 meV. Upon cooling, the characteristic changes in the experimental spectra can be described by a systematic reduction of the Fermi level. This finding is consistent with the ARPES study in Ref. [19] reporting a significant shift of the Fermi level at tem-

peratures above T_C . Aided by band-resolved optical conductivity calculations given in the Supplemental Material [36], the variation of the low-energy spectral weight can be related to changes of the transition energy between multiple linear Fe $3d$ -bands along $K \rightarrow \Gamma$, $\Gamma \rightarrow A$, and $A \rightarrow L$ [see Fig. 2 (e)]. Note that, for all calculations, the energy axis needs to be rescaled by 1/2.1 to achieve a good match with the experiment. A comparable rescaling factor of 1/1.6 was observed in ARPES measurements [20]. Moreover, a similar discrepancy between theory and experiment is reported for other magnetic kagome metals, such as the RMn_6Sn_6 family and $Co_3Sn_2S_2$, signaling a significant influence of electronic correlations [39, 44]. This effect is also observable in the difference between the experimental and DFT plasma frequencies, which can be used to gauge the strength of the electronic correlations as done in Fig. S8. Our data evidence much stronger correlations in FeGe compared to the nonmagnetic kagome metals, AV_3Sb_5 and ScV_6Sn_6 , and even compared to the magnetic $Co_3Sn_2S_2$.

Upon cooling below T_C , several modifications in the

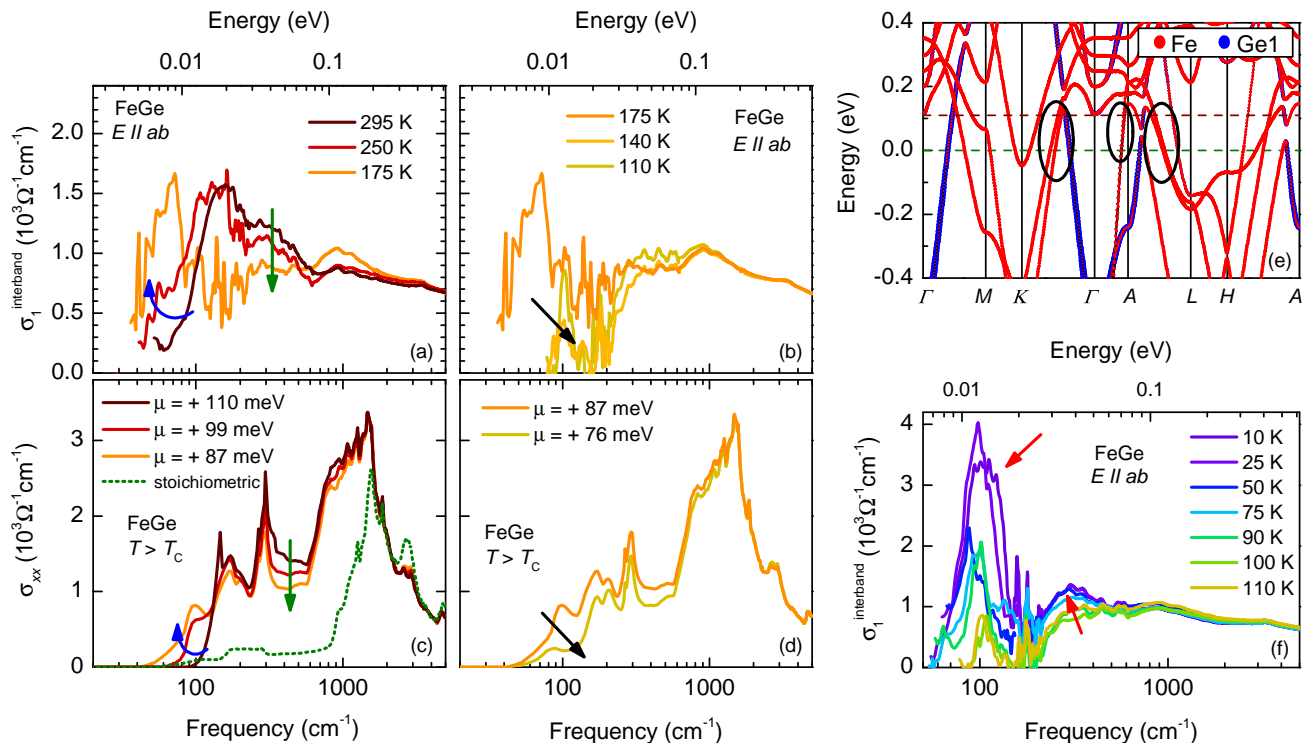


FIG. 2. (a) and (b) Experimental interband transitions of FeGe at temperatures above T_C , obtained by subtracting the Drude and localization peaks and the Fano resonance from the optical conductivity. (c) and (d) DFT optical conductivities for different electron dopings expressed by the chemical potential μ . The arrows mark characteristic changes in the spectra. (e) Calculated band structure for the high-temperature phase with colored dots symbolizing the contributions of different atoms. The black ovals highlight the linear Fe bands crossing the Fermi level responsible for the low-energy interband optical transitions. Dashed horizontal lines mark the position of the Fermi level for the stoichiometric case (green) and for $\mu = +110$ meV (brown), corresponding to room temperature. (f) Experimental interband transitions at temperatures below T_C . Red arrows mark the enhancement in the spectral weight at low energies due to the structural distortion.

electronic structure are clearly detected. First, the Fano resonance shifts to lower energies and significantly broadens upon approaching T_C , indicating strong electron-phonon coupling. This behavior is highly unusual for the temperature evolution of phonon modes, which are expected to sharpen and blueshift as the lattice hardens with decreasing temperature (see Supplemental Material for a more detailed discussion on the Fano resonance [36]). Second, there is a notable enhancement in the spectral weight around 250 cm^{-1} and a gradual formation of a sharp absorption feature at 100 cm^{-1} , as displayed in Fig. 2 (f). However, no spectral weight transfer from low to high energies, i.e., no optical signature of a CDW gap, is observed. The absence of a gap opening in the optical spectra is consistent with the results of the Raman studies [45].

To further investigate the effect of lattice distortion below T_C on the electronic structure, we carry out DFT calculations of the band structure and optical conductivity for the low-temperature phase. Below T_C , a $2 \times 2 \times 2$ superstructure as depicted in Fig. 1 (a), involving a tri-hexagonal (trh) distortion of the Fe-kagome planes was

observed by X-ray diffraction (XRD) measurements [19]. Additionally, a partial dimerization of Ge1 atoms was proposed by XRD and inelastic X-ray scattering studies on annealed samples, as well as DFT simulations [24, 25, 46–48]. In both cases, however, the distortion of the kagome planes is on the order of 10^{-4} \AA and, thus, extremely small.

The minuscule Fe displacement associated with the tri-hexagonal distortion induces only a tiny splitting between the parallel bands crossing the Fermi level (see Fig. S7 for a more detailed view). Thus, plenty of spectral weight is found at low energies, resulting in the pronounced peak at 100 cm^{-1} as displayed in Fig. 3 (b). The splitting between some parallel bands can be increased by imposing a larger displacement of the Fe atoms. As discussed in the Supplemental Material [36], this leads to more spectral weight at energies between 200 and 1000 cm^{-1} , with the low-energy peak at 100 cm^{-1} persisting. However, there is still no indication of a gap opening neither in the calculated optical conductivity nor in the density of states, as shown in Fig. S6. Hence, our study suggests a different nature of the low-temperature

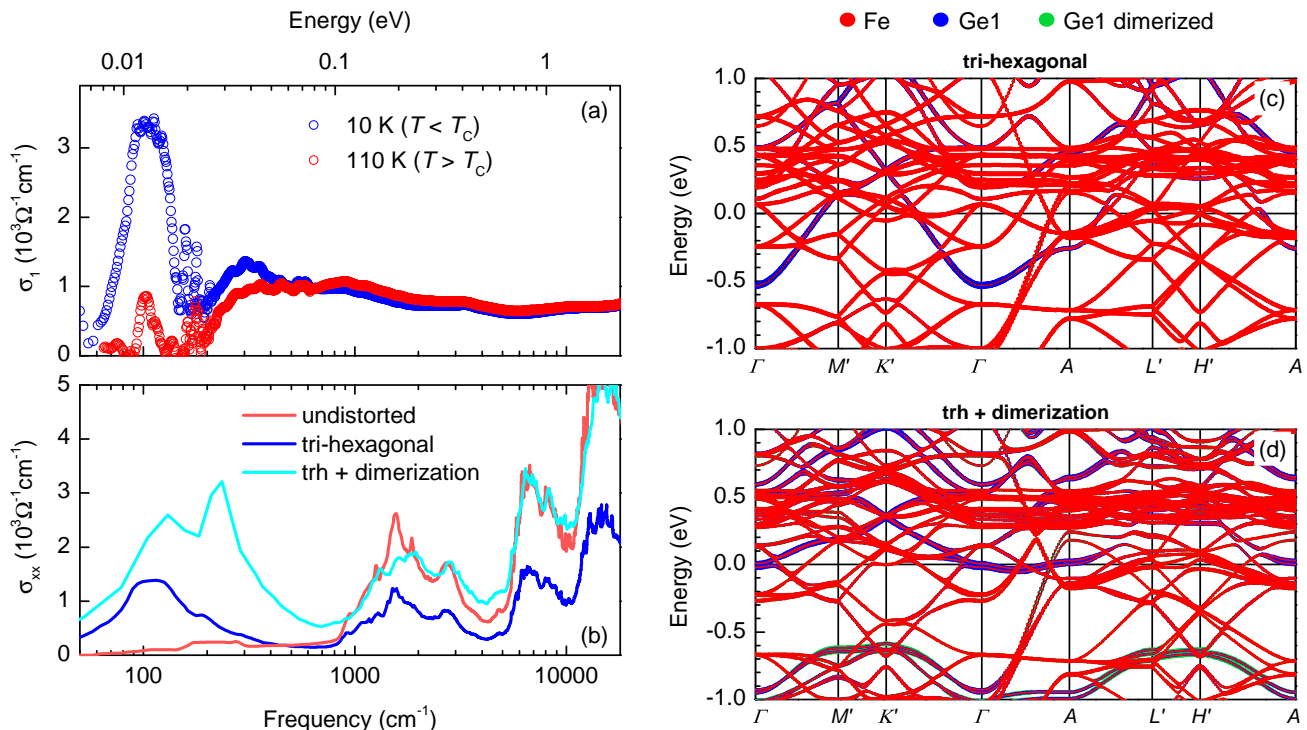


FIG. 3. (a) Experimental interband transitions of FeGe at 110 K (normal state) and 10 K (low-temperature state). (b) Calculated optical conductivity given for the normal state, as well as for the simple tri-hexagonal distortion of the kagome planes and the Ge-dimerized superstructure. Band structures of the low-temperature state for (c) the tri-hexagonal distortion of the kagome planes and (d) the Ge-dimerized superstructure. Colored dots show the contributions of different atoms.

transition in FeGe. Moreover, experimental manifestations of this transition appear to be dependent on the growth method and require sensitive measurements as it was not detected in early studies [22, 49]. Doping studies show a rapid suppression of the low-temperature anomaly in the magnetic susceptibility already at 1.5 % Sb-doping of the Ge-sites, militating in favor of the significant involvement of the Ge atoms in the low-temperature phase transition [50].

The Ge dimerization has a more drastic effect on the band structure compared to the deformation of the kagome planes. As seen in Fig. 2 (e) and Fig. 3 (c), precisely one in-plane Ge1 band crosses the Fermi level in the normal state. This band becomes split in the dimerized state with a gap of around 0.7 eV [panel (d)]. While contributions from this splitting to the optical data are masked by several other interband optical transitions due to the multi-band nature of FeGe, a reorganization of the Fe bands near E_F leads to additional spectral weight at approximately 250 cm^{-1} , consistent with the experimental result. Along with the improved agreement between theory and the experiment above 1000 cm^{-1} , these findings support the Ge dimerization scenario. Furthermore, the involvement of Ge1 atoms may also explain why the low-temperature transition has rather strong signatures in the optical spectra, i.e., Fano anomalies and differ-

ent interband transitions, even though almost no changes happen in the Fe-kagome planes.

The low-temperature anomaly in the magnetic susceptibility and the specific heat at T_C can be enhanced by a post-growth annealing process. However, the signature of the corresponding phase transition in the electric resistivity remains astonishingly weak [24, 25, 45]. While additional Bragg peaks below T_C imply a structural modulation [19], this does not necessarily lead to a CDW. Kagome systems are prone to multiple structural instabilities, such as Wigner crystallization [9, 14]. Moreover, breathing distortion of the kagome lattice is a well-known effect in quantum magnetism, but also in the kagome metals where Fe_3Sn_2 adopts the breathing structure without any CDW [51–54].

Overall, there is a sharp contrast between FeGe and other kagome metals exhibiting a CDW at low temperatures, including the renowned AV_3Sb_5 compounds. Their kagome planes exhibit a very similar structural distortion at low temperatures, forming a 2×2 in-plane superstructure. However, being on the order of 10^{-1} \AA , the atomic displacement is much more pronounced in the AV_3Sb_5 compounds [55]. Interestingly, in their normal state, all these kagome metals feature multiple d -bands and exactly one p -band crossing the Fermi level. This p -band is related to the in-plane Ge1 atoms in FeGe but to

out-of-plane Sb2 atoms in AV_3Sb_5 [56]. It essentially remains intact in the CDW phase of AV_3Sb_5 [55] but splits in FeGe due to the partial dimerization of the in-plane Ge1 atoms. Lastly, our data do not reveal the presence of a gap in the low-temperature phase of FeGe, while clear signatures of a gap opening in ScV_6Sn_6 and the AV_3Sb_5 compounds were detected by infrared spectroscopy [40–42, 57–60].

All these findings imply that the low-temperature phase of FeGe is substantially different from the CDW phase observed in other kagome metals. On the one hand, our study supports the partial dimerization of the in-plane Ge atoms, being decisive for the significant changes in the optical data below the anomaly at T_C . On the other hand, the absence of a gap in both experiment and theory is clearly different from the conventional CDW scenario that has been discussed for FeGe previously. Given the complex interplay between magnetism, structural instabilities, strong electronic correlations, as well as the simple tunability of the low-temperature anomaly by doping and annealing [24, 25, 45, 50], antiferromagnetic FeGe might open new routes to study so far unexplored regions in the rich phase diagram of kagome metals.

Authors acknowledge the fruitful discussions with S. Fratini and the technical support by G. Untereiner. M.W. is supported by IQST Stuttgart/Ulm via a project funded by the Carl Zeiss Stiftung. The work has been supported by the Deutsche Forschungsgemeinschaft (DFG) via DR228/51-3, DR228/68-1, and UY63/2-1.

* maxim.wenzel@pi1.physik.uni-stuttgart.de

- [1] I. Syôzi, Statistics of Kagomé Lattice, *Progress of Theoretical Physics* **6**, 306 (1951).
- [2] M. Mekata, Kagome: The Story of the Basketweave Lattice, *Physics Today* **56**, 12 (2003).
- [3] D. Kim and F. Liu, Realization of flat bands by lattice intercalation in kagome metals, *Phys. Rev. B* **107**, 205130 (2023).
- [4] Z. Li, J. Zhuang, L. Wang, H. Feng, Q. Gao, X. Xu, W. Hao, X. Wang, C. Zhang, K. Wu, S. X. Dou, L. Chen, Z. Hu, and Y. Du, Realization of flat band with possible nontrivial topology in electronic Kagome lattice, *Sci. Adv.* **4**, eaau4511 (2018).
- [5] M. L. Kiesel, C. Platt, and R. Thomale, Unconventional Fermi Surface Instabilities in the Kagome Hubbard Model, *Phys. Rev. Lett.* **110**, 126405 (2013).
- [6] K. Ferhat and A. Ralko, Phase diagram of the $\frac{1}{3}$ -filled extended Hubbard model on the kagome lattice, *Phys. Rev. B* **89**, 155141 (2014).
- [7] T. Neupert, M. M. Denner, J.-X. Yin, R. Thomale, and M. Z. Hasan, Charge order and superconductivity in kagome materials, *Nature Physics* **18**, 137 (2022).
- [8] F. Pollmann, P. Fulde, and K. Shtengel, Kinetic Ferromagnetism on a Kagome Lattice, *Phys. Rev. Lett.* **100**, 136404 (2008).
- [9] C. Wu, D. Bergman, L. Balents, and S. Das Sarma, Flat Bands and Wigner Crystallization in the Honeycomb Optical Lattice, *Phys. Rev. Lett.* **99**, 070401 (2007).
- [10] M. L. Kiesel and R. Thomale, Sublattice interference in the kagome Hubbard model, *Phys. Rev. B* **86**, 121105 (2012).
- [11] S.-L. Yu and J.-X. Li, Chiral superconducting phase and chiral spin-density-wave phase in a Hubbard model on the kagome lattice, *Phys. Rev. B* **85**, 144402 (2012).
- [12] Y.-P. Lin and R. M. Nandkishore, Complex charge density waves at Van Hove singularity on hexagonal lattices: Haldane-model phase diagram and potential realization in the kagome metals AV_3Sb_5 ($A=K, Rb, Cs$), *Phys. Rev. B* **104**, 045122 (2021).
- [13] L. Nie, K. Sun, W. Ma, D. Song, L. Zheng, Z. Liang, P. Wu, F. Yu, J. Li, M. Shan, D. Zhao, S. Li, B. Kang, Z. Wu, Y. Zhou, K. Liu, Z. Xiang, J. Ying, Z. Wang, T. Wu, and X. Chen, Charge-density-wave-driven electronic nematicity in a kagome superconductor, *Nature* **604**, 59 (2022).
- [14] Y. Chen, S. Xu, Y. Xie, C. Zhong, C. Wu, and S. B. Zhang, Ferromagnetism and Wigner crystallization in kagome graphene and related structures, *Phys. Rev. B* **98**, 035135 (2018).
- [15] B. R. Ortiz, L. C. Gomes, J. R. Morey, M. Winiarski, M. Bordelon, J. S. Mangum, I. W. H. Oswald, J. A. Rodriguez-Rivera, J. R. Neilson, S. D. Wilson, E. Ertekin, T. M. McQueen, and E. S. Toberer, New kagome prototype materials: discovery of KV_3Sb_5 , RbV_3Sb_5 , and CsV_3Sb_5 , *Phys. Rev. Mater.* **3**, 094407 (2019).
- [16] H. Tan, Y. Liu, Z. Wang, and B. Yan, Charge Density Waves and Electronic Properties of Superconducting Kagome Metals, *Phys. Rev. Lett.* **127**, 046401 (2021).
- [17] M. M. Denner, R. Thomale, and T. Neupert, Analysis of Charge Order in the Kagome Metal AV_3Sb_5 ($A = K, Rb, Cs$), *Phys. Rev. Lett.* **127**, 217601 (2021).
- [18] M. Kang, S. Fang, J. Yoo, B. R. Ortiz, Y. M. Oey, J. Choi, S. H. Ryu, J. Kim, C. Jozwiak, A. Bostwick, E. Rotenberg, E. Kaxiras, J. G. Checkelsky, S. D. Wilson, J.-H. Park, and R. Comin, Charge order landscape and competition with superconductivity in kagome metals, *Nat. Mater.* **22**, 186 (2022).
- [19] X. Teng, L. Chen, F. Ye, E. Rosenberg, Z. Liu, J.-X. Yin, Y.-X. Jiang, J. S. Oh, M. Z. Hasan, K. J. Neubauer, B. Gao, Y. Xie, M. Hashimoto, D. Lu, C. Jozwiak, A. Bostwick, E. Rotenberg, R. J. Birgeneau, J.-H. Chu, M. Yi, and P. Dai, Discovery of charge density wave in a kagome lattice antiferromagnet, *Nature* **609**, 490 (2022).
- [20] X. Teng, J. S. Oh, H. Tan, L. Chen, J. Huang, B. Gao, J.-X. Yin, J.-H. Chu, M. Hashimoto, C. Lu, Donghui Jozwiak, A. Bostwick, E. Rotenberg, G. E. Granroth, B. Yan, R. J. Birgeneau, P. Dai, and M. Yi, Magnetism and charge density wave order in kagome FeGe, *Nat. Phys.* **19**, 814 (2023).
- [21] J.-X. Yin, Y.-X. Jiang, X. Teng, M. S. Hossain, S. Mardanya, T.-R. Chang, Z. Ye, G. Xu, M. M. Denner, T. Neupert, B. Lienhard, H.-B. Deng, C. Setty, Q. Si, G. Chang, Z. Guguchia, B. Gao, N. Shumiya, Q. Zhang, T. A. Cochran, D. Multer, M. Yi, P. Dai, and M. Z. Hasan, Discovery of Charge Order and Corresponding Edge State in Kagome Magnet FeGe, *Phys. Rev. Lett.* **129**, 166401 (2022).
- [22] J. Bernhard, B. Lebeck, and O. Beckman, Neutron

- diffraction studies of the low-temperature magnetic structure of hexagonal FeGe, *J. Phys. F* **14**, 2379 (1984).
- [23] J. Bernhard, B. Lebeck, and O. Beckman, Magnetic phase diagram of hexagonal FeGe determined by neutron diffraction, *Journal of Physics F: Metal Physics* **18**, 539 (1988).
- [24] Z. Chen, X. Wu, S. Zhou, J. Zhang, R. Yin, Y. Li, M. Li, J. Gong, M. He, Y. Chai, X. Zhou, Y. Wang, A. Wang, Y.-J. Yan, and D.-L. Feng, Long-ranged charge order conspired by magnetism and lattice in an antiferromagnetic Kagome metal (2023), [arXiv:2307.07990](https://arxiv.org/abs/2307.07990).
- [25] C. Shi, Y. Liu, B. B. Maity, Q. Wang, S. R. Kotla, S. Ramakrishnan, C. Eisele, H. Agarwal, L. Noohinejad, Q. Tao, B. Kang, Z. Lou, X. Yang, Y. Qi, X. Lin, Z.-A. Xu, A. Thamizhavel, G.-H. Cao, S. van Smaalen, S. Cao, and J.-K. Bao, Disordered structure for long-range charge density wave order in annealed crystals of magnetic kagome FeGe (2023), [arXiv:2308.09034](https://arxiv.org/abs/2308.09034).
- [26] S. Wu, M. Klemm, J. Shah, E. T. Ritz, C. Duan, X. Teng, B. Gao, F. Ye, M. Matsuda, F. Li, X. Xu, M. Yi, T. Birol, P. Dai, and G. Blumberg, Symmetry breaking and ascending in the magnetic kagome metal FeGe (2023), [arXiv:2309.14314](https://arxiv.org/abs/2309.14314).
- [27] Y. Huang, H. P. Wang, W. D. Wang, Y. G. Shi, and N. L. Wang, Formation of the density wave energy gap in $\text{Na}_2\text{Ti}_2\text{Sb}_2\text{O}$: An optical spectroscopy study, *Phys. Rev. B* **87**, 100507 (2013).
- [28] W. J. Ban, H. P. Wang, C. W. Tseng, C. N. Kuo, C. S. Lue, and N. L. Wang, Revealing multiple charge-density-wave orders in TbTe_3 by optical conductivity and ultrafast pump-probe experiments, *Sci. China Phys. Mech.* **60**, 047011 (2017).
- [29] V. Vescoli, L. Degiorgi, H. Berger, and L. Forró, Dynamics of Correlated Two-Dimensional Materials: The $2H - \text{TaSe}_2$ Case, *Phys. Rev. Lett.* **81**, 453 (1998).
- [30] R. Y. Chen, S. J. Zhang, M. Y. Zhang, T. Dong, and N. L. Wang, Revealing Extremely Low Energy Amplitude Modes in the Charge-Density-Wave Compound LaAgSb_2 , *Phys. Rev. Lett.* **118**, 107402 (2017).
- [31] R. Y. Chen, B. F. Hu, T. Dong, and N. L. Wang, Revealing multiple charge-density-wave orders in TbTe_3 by optical conductivity and ultrafast pump-probe experiments, *Phys. Rev. B* **89**, 075114 (2014).
- [32] F. Pfuner, P. Lerch, J.-H. Chu, H.-H. Kuo, I. R. Fisher, and L. Degiorgi, Temperature dependence of the excitation spectrum in the charge-density-wave ErTe_3 and HoTe_3 systems, *Phys. Rev. B* **81**, 195110 (2010).
- [33] A. Perucchi, L. Degiorgi, and R. E. Thorne, Optical investigation of the charge-density-wave phase transitions in NbSe_3 , *Phys. Rev. B* **69**, 195114 (2004).
- [34] G. Grüner, *Density Waves In Solids* (CRC Press, 1994).
- [35] K. Momma and F. Izumi, *VESTA*: a three-dimensional visualization system for electronic and structural analysis, *J. Appl. Crystallogr.* **41**, 653 (2008).
- [36] See Supplemental Material at for experimental details, data analysis, details on DFT calculations, and additional computational results (see, also, references [61–74] therein).
- [37] A. Biswas, O. Iakutkina, Q. Wang, H. C. Lei, M. Dressel, and E. Uykur, Spin-Reorientation-Induced Band Gap in Fe_3Sn_2 : Optical Signatures of Weyl Nodes, *Phys. Rev. Lett.* **125**, 076403 (2020).
- [38] F. Schilberth, N. Unglert, L. Prodan, F. Meggle, J. Ebad Allah, C. A. Kuntscher, A. A. Tsirlin, V. Tsurkan, J. Deisenhofer, L. Chioncel, I. Kézsmárki, and S. Bordács, Magneto-optical detection of topological contributions to the anomalous Hall effect in a kagome ferromagnet, *Phys. Rev. B* **106**, 144404 (2022).
- [39] M. Wenzel, A. A. Tsirlin, O. Iakutkina, Q. Yin, H. C. Lei, M. Dressel, and E. Uykur, Effect of magnetism and phonons on localized carriers in the ferrimagnetic kagome metals GdMn_6Sn_6 and TbMn_6Sn_6 , *Phys. Rev. B* **106**, L241108 (2022).
- [40] M. Wenzel, B. R. Ortiz, S. D. Wilson, M. Dressel, A. A. Tsirlin, and E. Uykur, Optical study of RbV_3Sb_5 : Multiple density-wave gaps and phonon anomalies, *Phys. Rev. B* **105**, 245123 (2022).
- [41] E. Uykur, B. R. Ortiz, S. D. Wilson, M. Dressel, and A. A. Tsirlin, Optical detection of the density-wave instability in the kagome metal KV_3Sb_5 , *npj Quantum Mater.* **7**, 16 (2022).
- [42] E. Uykur, B. R. Ortiz, O. Iakutkina, M. Wenzel, S. D. Wilson, M. Dressel, and A. A. Tsirlin, Low-energy optical properties of the nonmagnetic kagome metal CsV_3Sb_5 , *Phys. Rev. B* **104**, 045130 (2021).
- [43] M. Wenzel, A. A. Tsirlin, F. Capitani, Y. T. Chan, B. R. Ortiz, S. D. Wilson, M. Dressel, and E. Uykur, Pressure evolution of electron dynamics in the superconducting kagome metal CsV_3Sb_5 , *npj Quantum Mater.* **8**, 45 (2023).
- [44] Y. Xu, J. Zhao, C. Yi, Q. Wang, Q. Yin, Y. Wang, X. Hu, L. Wang, E. Liu, G. Xu, L. Lu, A. A. Soluyanov, H. Lei, Y. Shi, J. Luo, and Z.-G. Chen, Electronic correlations and flattened band in magnetic Weyl semimetal candidate $\text{Co}_3\text{Sn}_2\text{S}_2$, *Nat. Commun.* **11**, 3985 (2020).
- [45] X. Wu, X. Mi, L. Zhang, X. Zhou, M. He, Y. Chai, and A. Wang, Annealing tunable charge density wave order in a magnetic kagome material FeGe (2023), [arXiv:2308.01291](https://arxiv.org/abs/2308.01291).
- [46] Y. Wang, Enhanced spin-polarization via partial Ge-dimerization as the driving force of the charge density wave in FeGe, *Phys. Rev. Mater.* **7**, 104006 (2023).
- [47] S. Shao, J.-X. Yin, I. Belopolski, J.-Y. You, T. Hou, H. Chen, Y. Jiang, M. S. Hossain, M. Yahyavi, C.-H. Hsu, Y. P. Feng, A. Bansil, M. Z. Hasan, and G. Chang, Intertwining of Magnetism and Charge Ordering in Kagome FeGe, *ACS Nano* **17**, 10164 (2023).
- [48] H. Miao, T. T. Zhang, H. X. Li, G. Fabbris, A. H. Said, R. Tartaglia, T. Yilmaz, E. Vescovo, J.-X. Yin, S. Murakami, X. L. Feng, K. Jiang, X. L. Wu, A. F. Wang, S. Okamoto, Y. L. Wang, and H. N. Lee, Signature of spin-phonon coupling driven charge density wave in a kagome magnet, *Nat. Commun.* **14**, 6183 (2023).
- [49] O. Beckman, K. Carrander, L. Lundgren, and M. Richardson, Susceptibility Measurements and Magnetic Ordering of Hexagonal FeGe, *Phys. Scr.* **6**, 151 (1972).
- [50] J. Huang, C. Shang, J. Qin, F. Pan, B. Shi, J. Wang, J. Liu, D. Xu, H. Zhang, H. Wang, L. Hao, and P. Cheng, $\text{FeGe}_{1-x}\text{Sb}_x$: a series of novel kagome metals with non-collinear antiferromagnetism (2023), [arXiv:2309.16502](https://arxiv.org/abs/2309.16502).
- [51] R. Schaffer, Y. Huh, K. Hwang, and Y. B. Kim, Quantum spin liquid in a breathing kagome lattice, *Phys. Rev. B* **95**, 054410 (2017).
- [52] H. Tanaka, Y. Fujisawa, K. Kuroda, R. Noguchi, S. Sakuragi, C. Bareille, B. Smith, C. Cacho, S. W. Jung, T. Muro, Y. Okada, and T. Kondo, Three-dimensional electronic structure in ferromagnetic Fe_3Sn_2 with breath-

- ing kagome bilayers, *Phys. Rev. B* **101**, 161114 (2020).
- [53] M. Hirschberger, T. Nakajima, S. Gao, L. Peng, A. Kikkawa, T. Kurumaji, M. Kriener, Y. Yamasaki, H. Sagayama, H. Nakao, K. Ohishi, K. Kakurai, Y. Taguchi, X. Yu, T.-h. Arima, and Y. Tokura, Three-dimensional electronic structure in ferromagnetic Fe_3Sn_2 with breathing kagome bilayers, *Nat. Commun.* **10**, 5831 (2019).
- [54] S. Regmi, T. Fernando, Y. Zhao, A. P. Sakhya, G. Dhakal, I. Bin Elius, H. Vazquez, J. D. Denlinger, J. Yang, J.-H. Chu, X. Xu, T. Cao, and M. Neupane, Spectroscopic evidence of flat bands in breathing kagome semiconductor Nb_3I_8 , *Commun. Mat.* **3**, 100 (2022).
- [55] B. R. Ortiz, S. M. L. Teicher, L. Kautzsch, P. M. Sarte, N. Ratcliff, J. Harter, J. P. C. Ruff, R. Seshadri, and S. D. Wilson, Fermi Surface Mapping and the Nature of Charge-Density-Wave Order in the Kagome Superconductor CsV_3Sb_5 , *Phys. Rev. X* **11**, 041030 (2021).
- [56] A. A. Tsirlin, P. Fertey, B. R. Ortiz, B. Klis, V. Merkl, M. Dressel, S. D. Wilson, and E. Uykur, Role of Sb in the superconducting kagome metal CsV_3Sb_5 revealed by its anisotropic compression, *SciPost Phys.* **12**, 49 (2022).
- [57] T. Hu, H. Pi, S. Xu, L. Yue, Q. Wu, Q. Liu, S. Zhang, R. Li, X. Zhou, J. Yuan, D. Wu, T. Dong, H. Weng, and N. Wang, Optical spectroscopy and band structure calculations of the structural phase transition in the vanadium-based kagome metal ScV_6Sn_6 , *Phys. Rev. B* **107**, 165119 (2023).
- [58] D. W. Kim, S. Liu, C. Wang, H. W. Nam, G. Pokharel, S. D. Wilson, J.-H. Cho, and S. J. Moon, Infrared probe of the charge density wave gap in ScV_6Sn_6 , *Phys. Rev. B* **108**, 205118 (2023).
- [59] X. Zhou, Y. Li, X. Fan, J. Hao, Y. Dai, Z. Wang, Y. Yao, and H.-H. Wen, Origin of charge density wave in the kagome metal CsV_3Sb_5 as revealed by optical spectroscopy, *Phys. Rev. B* **104**, L041101 (2021).
- [60] X. Zhou, Y. Li, X. Fan, J. Hao, Y. Xiang, Z. Liu, Y. Dai, Z. Wang, Y. Yao, and H.-H. Wen, Electronic correlations and evolution of the charge density wave in the kagome metals AV_3Sb_5 ($A = \text{K}, \text{Rb}, \text{Cs}$), *Phys. Rev. B* **107**, 165123 (2023).
- [61] M. W. Richardson, N. Ingri, P. Salomaa, G. D. Bloom, and G. Hagen, The Partial Equilibrium Diagram of the Fe-Ge System in the Range 40-72 at. % Ge, and the Crystallisation of some Iron Germanides by Chemical Transport Reactions, *Acta Chem. Scand.* **21**, 2305 (1967).
- [62] C. C. Homes, M. Reedyk, D. A. Cradles, and T. Timusk, Technique for measuring the reflectance of irregular, submillimeter-sized samples, *Appl. Opt.* **32**, 2976 (1993).
- [63] D. B. Tanner, Use of x-ray scattering functions in Kramers-Kronig analysis of reflectance, *Phys. Rev. B* **91**, 035123 (2015).
- [64] P. Blaha, K. Schwarz, G. Madsen, D. Kvasnicka, J. Luitz, R. Laskowski, F. Tran, and L. Marks, WIEN2k, An Augmented Plane Wave + Local Orbitals Program for Calculating Crystal Properties (Karlheinz Schwarz, Techn. Universität Wien, Austria), 2018. ISBN 3-9501031-1-2.
- [65] P. Blaha, K. Schwarz, F. Tran, R. Laskowski, G. K. H. Madsen, and L. D. Marks, WIEN2k: An APW+lo program for calculating the properties of solids, *J. Chem. Phys.* **152**, 074101 (2020).
- [66] J. P. Perdew, K. Burke, and M. Ernzerhof, Generalized Gradient Approximation Made Simple, *Phys. Rev. Lett.* **77**, 3865 (1996).
- [67] G. Kresse and J. Furthmüller, Efficient iterative schemes for ab initio total-energy calculations using a plane-wave basis set, *Phys. Rev. B* **54**, 11169 (1996).
- [68] C. Ambrosch-Draxl and J. O. Sofo, Linear optical properties of solids within the full-potential linearized augmented planewave method, *Comput. Phys. Commun.* **175**, 1 (2006).
- [69] S. Fratini, S. Ciuchi, and D. Mayou, Phenomenological model for charge dynamics and optical response of disordered systems: Application to organic semiconductors, *Phys. Rev. B* **89**, 235201 (2014).
- [70] U. Fano, Effects of Configuration Interaction on Intensities and Phase Shifts, *Phys. Rev.* **124**, 1866 (1961).
- [71] H. Rammal, A. Ralko, S. Ciuchi, and S. Fratini, Transient localization from the interaction with quantum bosons (2023), [arXiv:2312.03840](https://arxiv.org/abs/2312.03840).
- [72] M. Kawamura, FermiSurfer: Fermi-surface viewer providing multiple representation schemes, *Comput. Phys. Commun.* **239**, 197 (2019).
- [73] M. Dressel and G. Grüner, *Electrodynamics of Solids: Optical Properties of Electrons in Matter* (Cambridge University Press, 2002).
- [74] Y. Shao, A. N. Rudenko, J. Hu, Z. Sun, Y. Zhu, S. Moon, A. Millis, S. Yuan, A. I. Lichtenstein, D. Smirnov, Z. Q. Mao, M. I. Katsnelson, and D. N. Basov, Electronic correlations in nodal-line semimetals, *Nat. Phys.* **16**, 636 (2020).

Supplemental materials for "Intriguing low-temperature state in the antiferromagnetic kagome metal FeGe"

M. Wenzel, E. Uykur, A. A. Tsirlin, S. Pal, R. Mathew Roy, C. Yi, C. Shekhar, C. Felser, A. V. Pronin, M. Dressel

CRYSTAL GROWTH

B35-type FeGe single crystals are cultivated via the chemical vapor transport method, which employs iodine as a transport agent [S1]. High-purity Fe and Ge powders are combined and ground in an agate mortar bowl with a molar ratio of Fe:Ge = 1:1. The mixture and iodine ($\sim 10 \text{ mg/cm}^3$) are then loaded into a quartz tube and sealed under high vacuum. After that, the tube is placed in a two-zone furnace with the source powder at 893 K and the crystallization region at 833 K. After one month of maintenance, shiny crystals in the form of hexagonal prisms are produced at the cold end.

EXPERIMENTAL DETAILS

Temperature- and frequency-dependent reflectivity measurements in the ab -plane were performed on a freshly cleaved sample with the lateral dimensions of $\sim 0.5 \times 1 \text{ mm}^2$ and thickness of about $400 \mu\text{m}$, as presented in Fig. S1 (a). For high energies ($600 \text{ cm}^{-1} \leq \omega \leq 18000 \text{ cm}^{-1}$), a Vertex80v spectrometer coupled to a Hyperion IR microscope was used, while the low-energy range ($50 \text{ cm}^{-1} \leq \omega < 600 \text{ cm}^{-1}$) was measured with an IFS113v spectrometer and a custom-built cryostat. Freshly evaporated gold mirrors served as the reference throughout the measurements. The absolute value of the reflectivity is deduced with the gold-overcoating technique as described in Ref. [S2] in the far-infrared range.

The optical conductivity is calculated from the measured in-plane reflectivity spectra employing standard Kramers-Kronig analysis. Below 50 cm^{-1} , the Hagen-Rubens relation is utilized for the data extrapolation, while x-ray scattering functions are used for the high-energy extrapolations [S3].

Prior to the optical measurements, the low-temperature anomaly at $T_C = 102 \text{ K}$ was confirmed by dc magnetic susceptibility measurements in zero field cooling (ZFC) and field cooling (FC) regimes with $\mu_0 H = 0.1 \text{ T}$. Additionally, four-point resistivity measurements were performed on the same sample piece as used for the optical experiments.

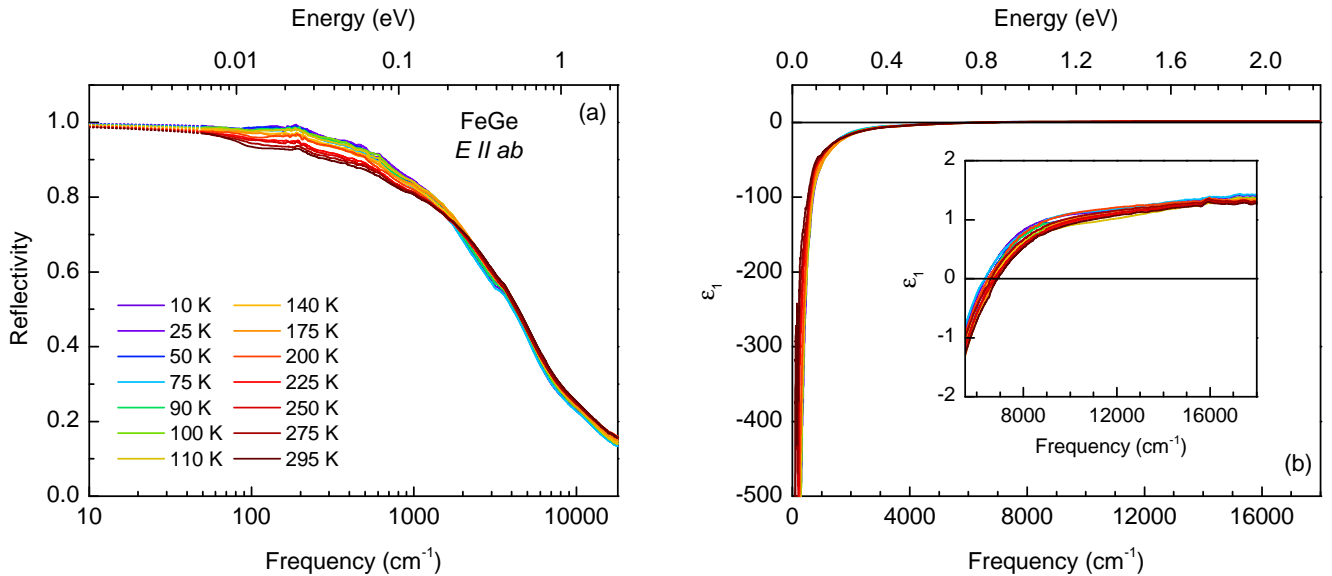


FIG. S1. (a) Temperature-dependent reflectivity over a broad frequency range measured in the ab -plane. Dotted lines are the Hagen-Rubens extrapolation to low energies. (b) Calculated dielectric permittivity. The inset highlights the zero crossing, marking the screened plasma frequency.

The obtained curve matches well with the dc resistivity values obtained from the Hagen-Rubens fits (see Fig. 1 (b) in the main text).

DFT CALCULATIONS

Band structure and optical conductivity calculations were performed in the WIEN2K code [S4, S5] using the Perdew-Burke-Ernzerhof flavor of the exchange-correlation potential [S6]. Spin-orbit coupling was included in all calculations. Experimental magnetic configuration was used, with ferromagnetic kagome layers coupled antiferromagnetically. For the normal state, experimental lattice parameters and atomic positions from Ref. [S7] were used, whereas the dimerized structure was taken from Ref. [S8] where it has been obtained by a structural relaxation in the VASP code [S9]. Experimental low-temperature structure with the tri-hexagonal distortion was taken from Ref. [S7]. The dimerization was added to it using the Ge1 positions from Ref. [S8]. Self-consistent calculations were converged on the k -mesh with $21 \times 21 \times 11$ points for the normal state and $12 \times 12 \times 13$ points for the low-temperature state. Optical conductivity was calculated using the `optic` module of WIEN2K [S10] on the dense k -mesh with up to $58 \times 58 \times 29$ points (normal state) and $36 \times 36 \times 38$ points (low-temperature state). Γ -point phonons were calculated in VASP using the frozen-phonon method.

DECOMPOSITION

Different contributions to the total optical conductivity are modeled with the Drude-Lorentz approach. The dielectric function [$\tilde{\epsilon} = \epsilon_1 + i\epsilon_2$] is expressed as

$$\tilde{\epsilon}(\omega) = \epsilon_\infty - \frac{\omega_{p,\text{Drude}}^2}{\omega^2 + i\omega/\tau_{\text{Drude}}} + \sum_j \frac{\Omega_j^2}{\omega_{0,j}^2 - \omega^2 - i\omega\gamma_j}, \quad (\text{S1})$$

with ϵ_∞ being the high-energy contributions to the real part of the dielectric permittivity. As plotted in Fig. S1 (b), these contributions are temperature-independent and approach the value of approximately 1.3. The other parameters $\omega_{p,\text{Drude}}$ and $1/\tau_{\text{Drude}}$ are the plasma frequency and the scattering rate of the itinerant carriers, respectively. Lorentzians described by the resonance frequency $\omega_{0,j}$, the strength of the oscillation Ω_j , and the width γ_j are used to model the interband absorptions.

The complex optical conductivity [$\tilde{\sigma} = \sigma_1 + i\sigma_2$] is calculated as

$$\tilde{\sigma}(\omega) = -i\omega\epsilon_0[\tilde{\epsilon}(\omega) - \epsilon_\infty], \quad (\text{S2})$$

with ϵ_0 being the vacuum permittivity.

Optical spectra of kagome metals are characterized by a broad absorption peak at low energies, which is intraband in nature, signaling the presence of charge carriers with hindered dynamics. In addition to the classical Drude-Lorentz approach, we use the displaced Drude peak formalism proposed in 2014 by Fratini *et al.* [S11] to model this so-called localization peak. Here, interactions of charge carriers with low-energy degrees of freedom, such as phonons and electric or magnetic fluctuations, can lead to a backscattering of the electrons, expressed by the backscattering time τ_b . The resulting localization effect shifts the classical Drude peak at zero frequency to a finite value.

$$\tilde{\sigma}_{\text{localization}}(\omega) = \frac{C}{\tau_b - \tau} \frac{\tanh\{\frac{\hbar\omega}{2k_B T}\}}{\hbar\omega} \cdot \text{Re} \left\{ \frac{1}{1 - i\omega\tau} - \frac{1}{1 - i\omega\tau_b} \right\}. \quad (\text{S3})$$

Here, C is a constant, \hbar is the reduced Planck constant, k_B the Boltzmann constant, and τ the elastic scattering time of the standard Drude model. At low temperatures, this peak becomes too sharp to be fitted with the displaced Drude peak. Hence, a regular Lorentzian is used to model this absorption.

The asymmetric phonon mode, at approximately 190 cm^{-1} , is reproduced most accurately by the Fano model

$$\sigma_1(\omega) = \frac{\sigma_0\omega\gamma[\gamma\omega(q^2 - 1) + 2q(\omega^2 - \omega_0^2)]}{4\pi[(\omega^2 - \omega_0^2)^2 + \gamma^2\omega^2]}. \quad (\text{S4})$$

This model can be considered a modified Lorentzian with an additional parameter, q . This dimensionless coupling parameter determines the coupling to the electronic background, leading to the asymmetry of the mode [S12].

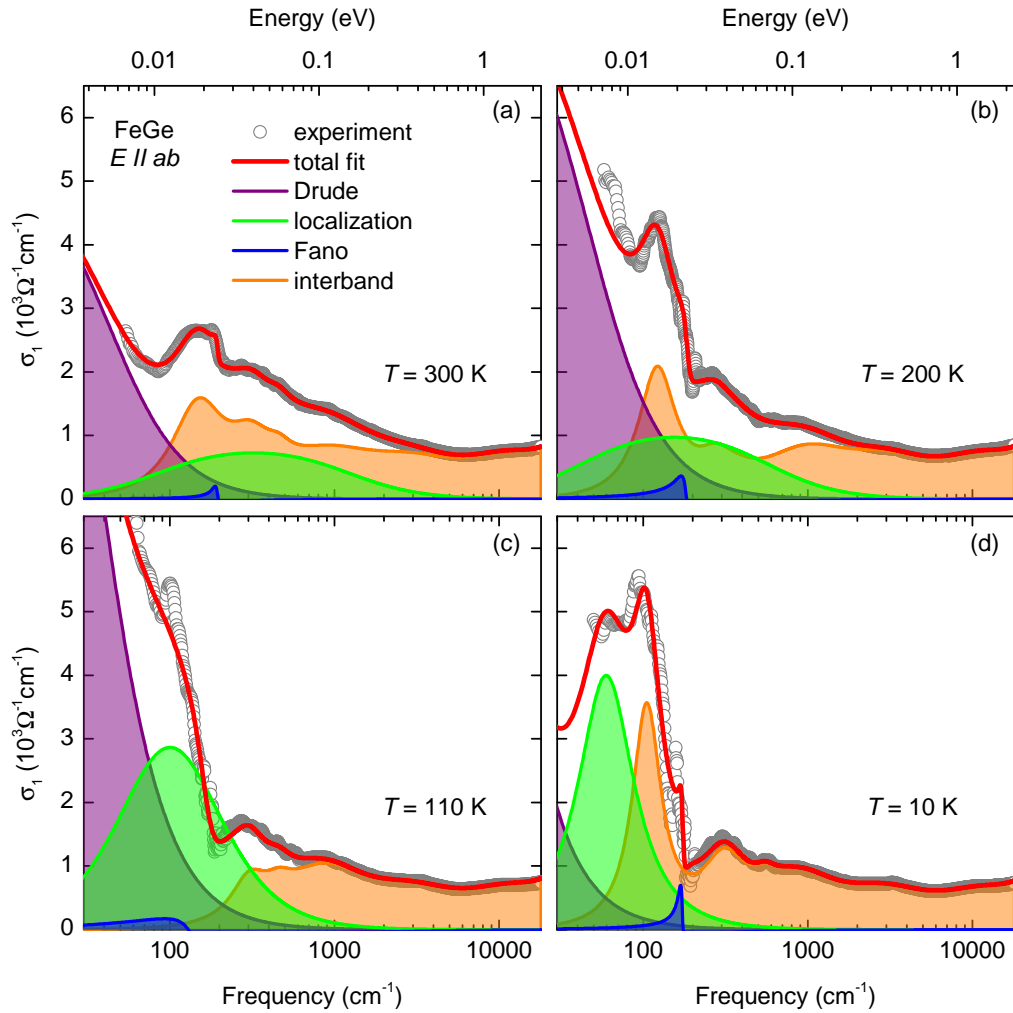


FIG. S2. Decomposed optical conductivities at several temperatures above and below the low-temperature anomaly, consisting of a Drude peak (purple), a localization peak (green), a Fano resonance (blue), and several interband transitions (orange) modeled with the Drude-Lorentz approach.

The total optical conductivity takes the form

$$\tilde{\sigma}(\omega) = \underbrace{\tilde{\sigma}_{\text{Drude}} + \tilde{\sigma}_{\text{localization}}}_{\text{intraband}} + \underbrace{\tilde{\sigma}_{\text{Fano}}}_{\text{phonon}} + \underbrace{\tilde{\sigma}_{\text{Lorentzians}}}_{\text{interband}}. \quad (\text{S5})$$

To ensure the reliability of the fit parameters, the reflectivity, and the complex optical conductivity are fitted simultaneously. Fig. S2 displays the decomposed real part of the optical conductivity at selected temperatures. The temperature evolution of the localization peak and the Fano antiresonance are discussed in the upcoming sections in more depth.

LOCALIZATION PEAK

The occurrence of a localization peak is a common feature among kagome metals. Upon cooling, this peak shows a pronounced linear redshift and may eventually merge with the conventional Drude peak at low temperatures, but also a saturation of the peak position at finite frequencies has been observed in some of the compounds. In the ferromagnetic Fe_3Sn_2 , the onset of saturation coincides with a reorientation of the magnetic moments [S13]. On the other hand, an interplay with a phonon mode was deemed to be the most likely scenario for the observed saturation in

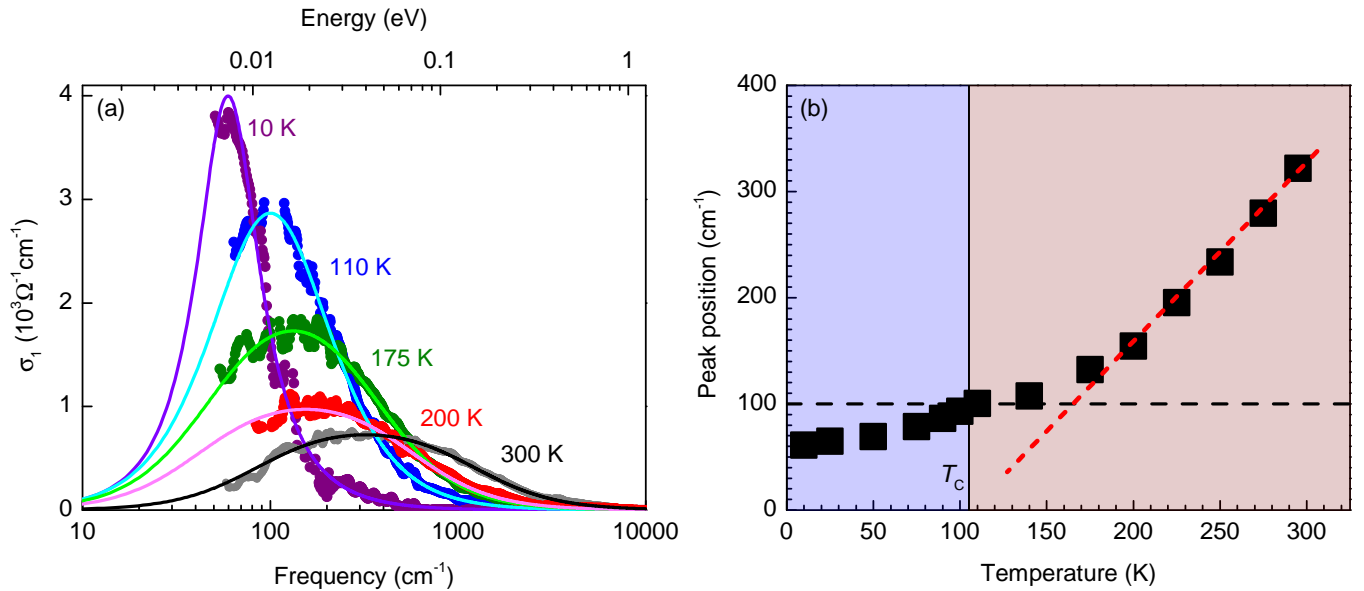


FIG. S3. (a) Temperature dependence of the localization peak shown after subtracting all other contributions from the experimental optical conductivity. Solid lines are the Fratini model fits. (b) Peak position as a function of temperature. The red- and blue-shaded areas separate the high- and low-temperature phases. The red dashed line demonstrates the linear redshift at high temperatures, while the black dashed line marks the saturation frequency of the high-temperature phase.

ferromagnetic GdMn_6Sn_6 [S14]. Moreover, a pinning of the localization peak was also reported in the non-magnetic KV_3Sb_5 , where the CDW transition temperature coincides with the onset of saturation [S15].

The temperature evolution of the localization peak in FeGe is given in Fig. S3. A linear redshift is observed at high temperatures, indicated by the red dashed line in panel (b). Below approximately 175 K, a deviation from the linear shift is detected, with the peak position saturating around 100 cm^{-1} . Given the absence of any magnetic or structural transition at such high temperatures, the most plausible explanation of such a behavior is the involvement of a phonon mode.

Indeed, in the framework of the displaced Drude peak (DDP) formalism by Fratini *et al.*, the localization peak would shift to lower energies upon cooling and pin to ω_0 due to interactions between the localized carriers and a static bosonic mode at ω_0 [S11, S16]. Moreover, as temperature decreases, a sharpening and gain of intensity are predicted by theory and indeed observed experimentally in FeGe. Below T_C , the localization peak becomes so sharp that it cannot be modeled with the displaced Drude peak anymore. Hence, we used a standard Lorentzian to fit the low-temperature data. A comparable sharpening of the localization peak was also reported in Fe_3Sn_2 at low temperatures [S13].

Below T_C , the peak shifts to slightly lower energies. This shift may be related to a modification of the phonon energy due to the structural distortion below T_C , assuming a phonon-mediated scenario. On the other hand, the sudden sharpening of the Fano resonance below T_C (seen Fig. S4 (e)) indicates a weakening of the electron-phonon coupling in the low-temperature phase. Moreover, assuming the coupling to phonons, the spectral weight of the localization peak can be used as a gauge of the electron-phonon coupling strength [S17]. As seen in Fig. S8 (a), this spectral weight is significantly reduced below T_C , suggesting a reduction of electron-phonon coupling in the low-temperature phase.

FANO RESONANCE

Fig. S4 (b) displays the Fano resonance, obtained after subtracting the intra- and interband contributions from the optical conductivity. The observed Fano mode around 190 cm^{-1} shows significant changes across T_C . We note that the mode is an antiresonance, and consequently, the coupling parameter q takes negative values. The strong anomalies become even more apparent when looking at the fit parameters given in panels (c)-(f). At high temperatures, a redshift of the resonance frequency ω_0 is accompanied by an increase of the intensity σ_0 . Most surprisingly, the Fano resonance reveals a notable broadening upon cooling, which is highly unexpected with decreasing thermal effects. The

coupling constant, which also determines the asymmetry of the resonance, indicates a decreasing asymmetry upon cooling with the minimum at T_C . Upon further cooling, the mode becomes more asymmetric and suddenly sharpens again. Together with the almost constant values of the resonance frequency below T_C , the temperature evolution of ω_0 strongly resembles the behavior of the localization peak, further supporting the coupling scenario between localized carriers and phonons.

The occurrence of an asymmetric phonon mode in the optical spectra of kagome metals is not exclusive to FeGe. A Fano resonance was also reported in the optical spectra of ScV_6Sn_6 , KV_3Sb_5 , and RbV_3Sb_5 , all three being kagome metals with a CDW phase at low temperatures. In ScV_6Sn_6 and FeGe, this mode sits at fairly low energies ($\sim 190 \text{ cm}^{-1}$) and can be associated with one of the infrared active E_{1u} modes according to our DFT calculations of FeGe given in Fig. S4 (a). In contrast, the interpretation of the Fano resonance in the AV_3Sb_5 compounds is not so straightforward, as it sits at much higher energies, where no more IR-active phonons are expected [S15, S18].

BAND-RESOLVED OPTICAL CONDUCTIVITY

As discussed in the main text, the highly temperature-sensitive interband transitions with $\omega \leq 200 \text{ cm}^{-1}$ above T_C are one of the key features in the optical spectra of FeGe. We have performed band-resolved optical conductivity calculations to relate these low-energy absorptions with specific transitions in the band structure. Due to the large amount of bands crossing E_F , the Fermi surface, given in Fig. S5 (f), is highly sensitive to the position of the Fermi level. Electron doping results in an upward shift of the Fermi level, allowing transitions at very low energies. As seen in Fig. S5 (a-d), these low-energy absorptions are mainly related to transitions between bands C and D, following the labeling in panel (e). Along $K \rightarrow \Gamma$, these bands are almost parallel and become closer when shifting the Fermi level upwards.

ADDITIONAL COMPUTATIONAL RESULTS

The absence of a gap in the experimental and the theoretical optical conductivity is also paralleled by the density of states (DOS) given in Fig. S6 (c) and (e) for the dimerized and simple tri-hexagonal distortion, respectively. For both superstructures, only a small reduction in the number of states near E_F is found. In addition to the tri-hexagonal distortion of the kagome layers, a star-of-David-type (soD) distortion as observed in CsV_3Sb_5 could be envisaged [S8, S20]. With the partially dimerized Ge atoms, the optical conductivity of the soD kagome distortion resembles the conductivity in the case of the tri-hexagonal distortion with overall smaller absolute values as shown in Fig. S6 (a). Given the better agreement between the optical conductivities in the normal state and in the case of the tri-hexagonal distortion at high energies, we deem the soD-type distortion of the kagome planes less likely in FeGe.

In comparison with other kagome metals exhibiting charge order, the in-plane distortion of the Fe-kagome layers detected by XRD measurements is extremely small [S7]. Hence, the main effect of this distortion is a tiny splitting between the parallel bands crossing the Fermi level, as highlighted in Fig. S7. We further explore the influence of the kagome distortion by imposing a larger Fe displacement similar to the AV_3Sb_5 compounds [S21]. This indeed increases the splitting between a few parallel bands crossing the Fermi level. However, only some additional spectral weight at frequencies above 100 cm^{-1} is produced, as shown in Fig. S6 (b). Consequently, there is still no observable spectral weight transfer from low to high energies that would indicate the opening of a gap below T_C . In fact, with two distinct low-energy absorptions at 100 cm^{-1} and 250 cm^{-1} , the calculated optical conductivity resembles the optical conductivities of the dimerized superstructures given in Fig. S6 (a). The DOS in panel (f) verifies the absence of a gap as no reduction of the states near E_F is observed.

PLASMA FREQUENCY AND ELECTRONIC CORRELATIONS

The experimental plasma frequencies are obtained from the spectral weight (SW) analysis of the Drude and localization peaks according to

$$\omega_p = \sqrt{\text{SW}_{\text{Drude}} + \text{SW}_{\text{loc}}}. \quad (\text{S6})$$

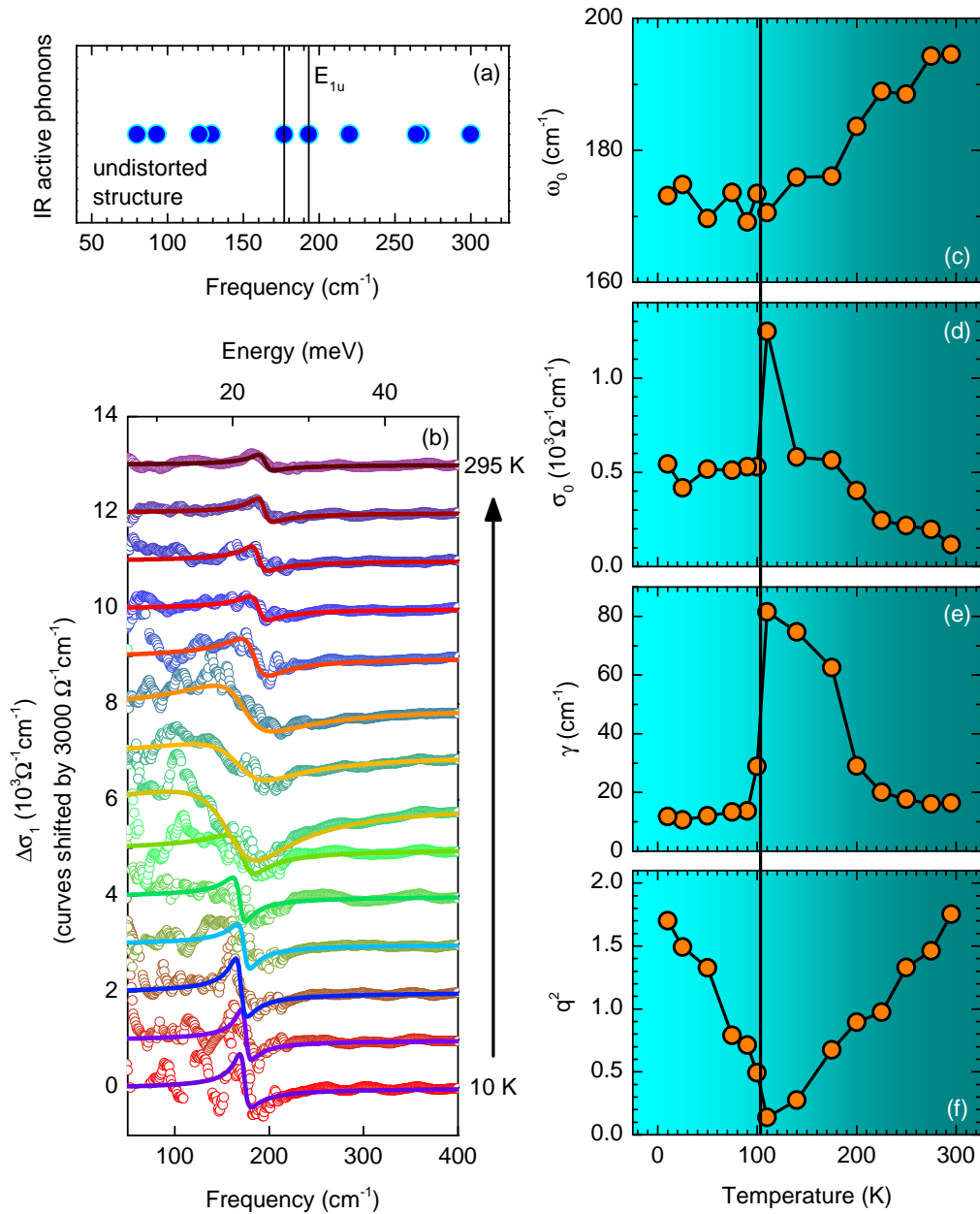


FIG. S4. (a) Infrared-active phonon frequencies calculated for the undistorted structure. Vertical lines mark the two E_{1u} modes with a comparable energy to the experimentally observed Fano resonance. (b) Low-energy optical conductivity, highlighting the Fano antiresonance. The spectra are presented as $\Delta\sigma_1(\omega)$ with all other contributions subtracted and the baselines shifted by $3000 \Omega^{-1} \text{cm}^{-1}$ for clarity. The solid lines are fits to the optical conductivity with the fit parameters given in (c)–(f). The vertical black line marks the anomaly at $T_C = 102$ K.

The spectral weight is calculated from the optical data by integrating the real part of the optical conductivity of the fitted Drude and localization peaks [S22]

$$\text{SW} = \frac{1}{\pi^2 \epsilon_0 c} \int_0^{\omega_c} \sigma_1(\omega) d\omega, \quad (\text{S7})$$

with c being the speed of light. The cut-off frequency is chosen as $\omega_c = 50000 \text{ cm}^{-1}$, considering the high-energy tail of the localization peak.

The temperature evolution of the intraband spectral weight is given in Fig. S8 (a). Above T_C , there is a spectral weight transfer between the Drude and the localization peaks, while the total SW can be considered constant within

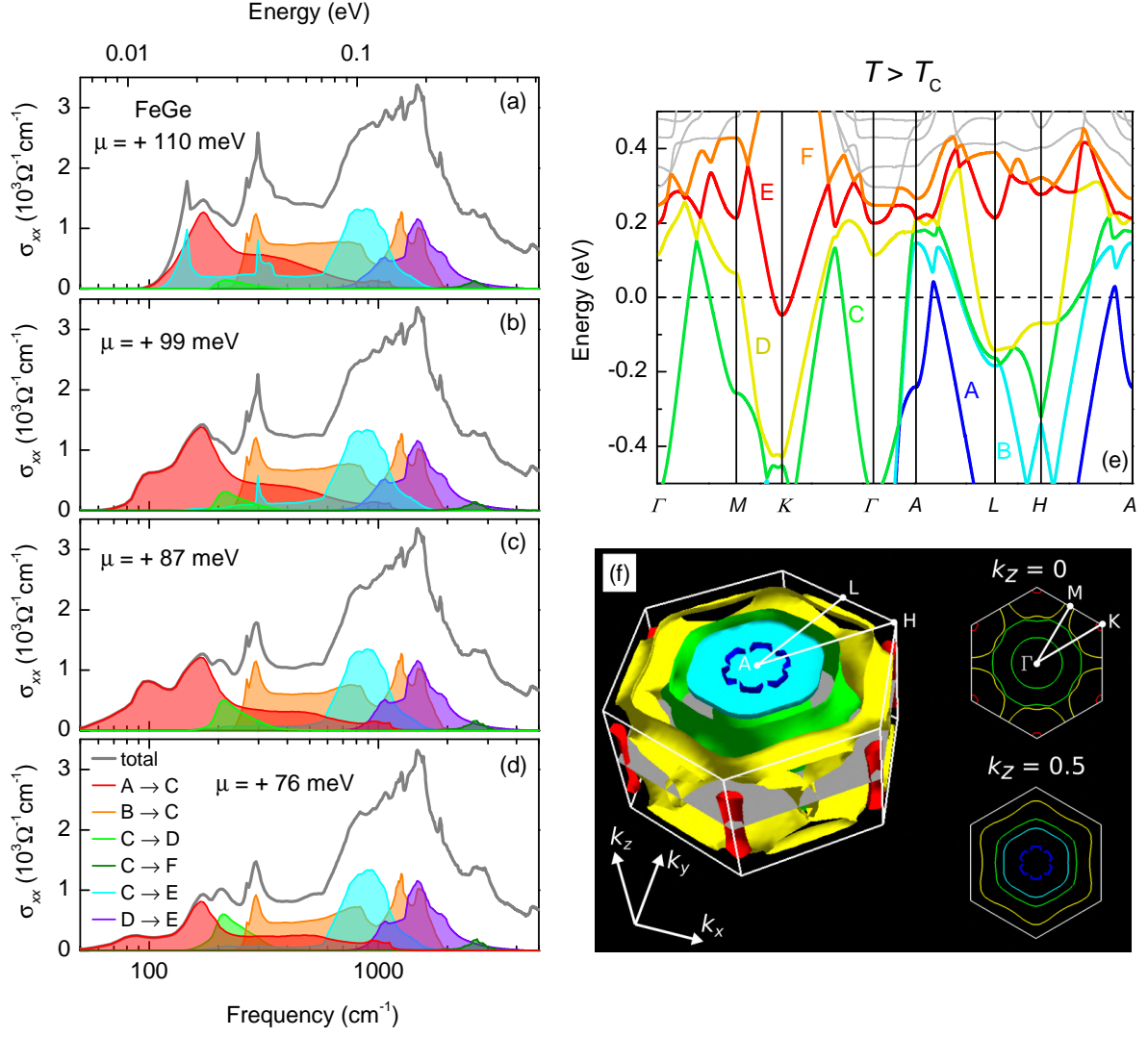


FIG. S5. (a)-(d) Band-resolved optical conductivity given for different electron dopings expressed by the chemical potential μ . Colors represent contributions from interband optical transitions between different bands according to the labeling in panel (e), showing the band structure for the normal state. (f) Fermi surface constructed from the calculated band structure and cuts along $k_z = 0$ and $k_z = 0.5$. *FermiSurfer* program was used for the visualization [S19].

the error bars. Below 110 K, the spectral weight of both intraband contributions is reduced, leading to a drop in the total SW and, consequently, in the plasma frequency. The plasma frequency can be written as $\omega_p \propto n/m^*$, with n being the carrier density and m^* the effective mass [S22]. Consequently, the decrease of ω_p below T_C can be attributed to either decreasing carrier density or increasing effective mass. Given the splitting between parallel bands crossing the Fermi level, as well as the splitting of the Ge1-band in the dimerized case, the effective mass is likely to be affected by the reconstruction of bands due to the structural transition.

The large rescaling factor of the energy axis needed to match the DFT calculations with the experimental results indicates the presence of considerable electronic correlations. The strength of electronic correlations can be estimated by the ratio $\omega_{p,\text{experiment}}^2/\omega_{p,\text{DFT}}^2$ [S24]. Using the experimental plasma frequency at 110 K and the DFT calculations with the Fermi level shifted by +76 meV, a value of approximately 0.17 is obtained. Note that this value is only slightly affected by the exact position of the Fermi level. Such a small value signals strong electronic correlations in the same range as observed for the RMn_6Sn_6 ($R = \text{Gd, Tb}$) compounds [S14]. In contrast, relatively moderate to almost absent electronic correlations are found in ScV_6Sn_6 and the AV_3Sb_5 compounds [S18, S23].

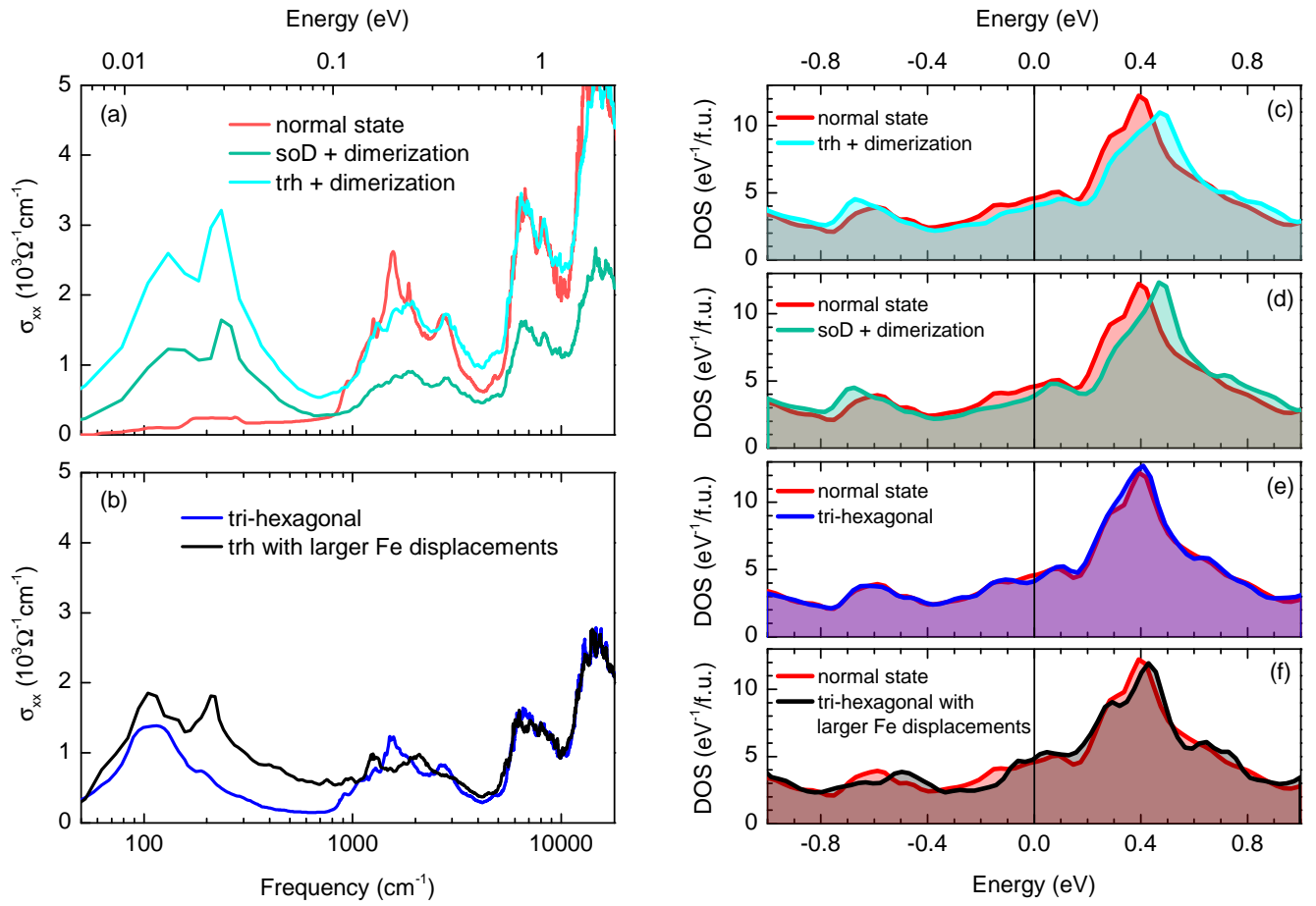


FIG. S6. (a) Comparison of calculated optical conductivities for the dimerized superstructures with a tri-hexagonal and star-of-David-type distortion of the Fe-kagome planes. (b) Calculated optical conductivities for the tri-hexagonal in-plane distortion with different Fe displacements as explained in the text. (c-f) Corresponding density of states overlapped with the density of states for the normal state without shifting the Fermi level.

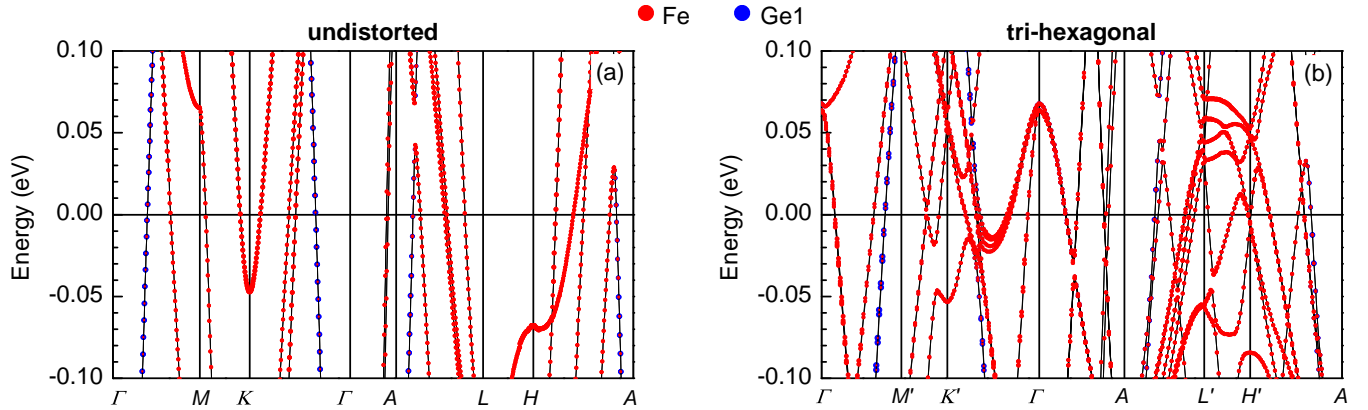


FIG. S7. Band dispersions nearby the Fermi level for the normal state (a) and the tri-hexagonal distortion (b). Colored dots show contributions of the Fe atoms (red) and Ge1 atoms (blue).

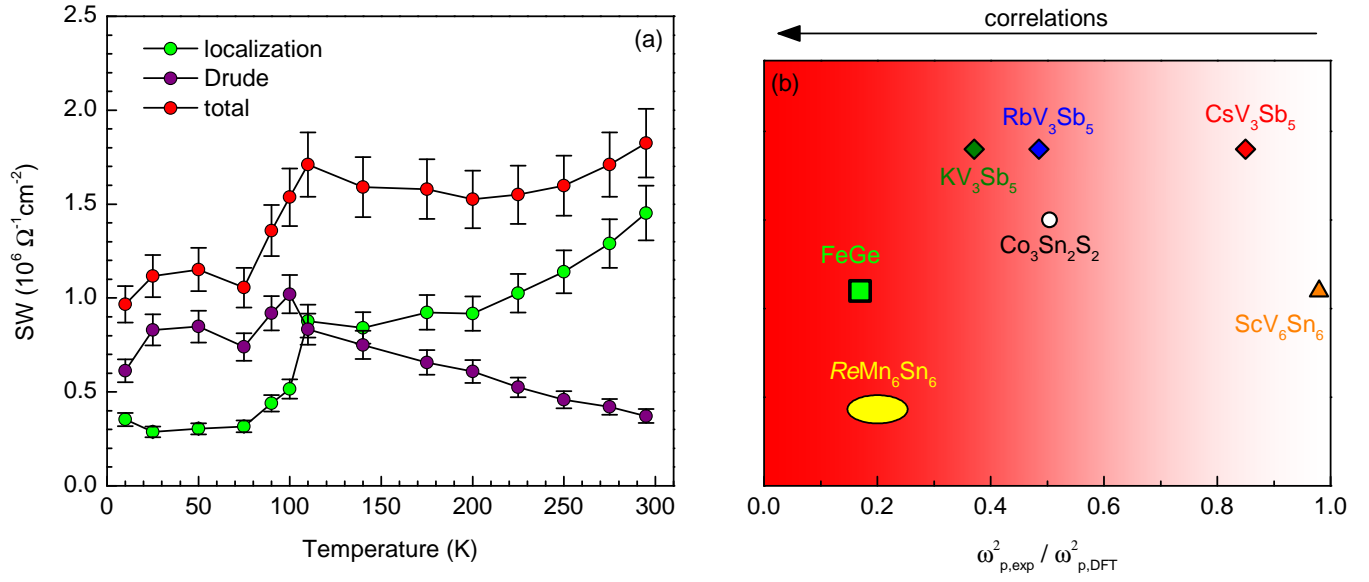


FIG. S8. (a) Temperature evolution of the intraband spectral weight. (b) Strength of electronic correlations for different kagome metals taken from Refs. [S14, S18, S23, S24].

-
- [S1] M. W. Richardson, N. Ingrid, P. Salomaa, G. D. Bloom, and G. Hagen, The Partial Equilibrium Diagram of the Fe-Ge System in the Range 40-72 at. % Ge, and the Crystallisation of some Iron Germanides by Chemical Transport Reactions, *Acta Chem. Scand.* **21**, 2305 (1967).
- [S2] C. C. Homes, M. Reedyk, D. A. Cradles, and T. Timusk, Technique for measuring the reflectance of irregular, submillimeter-sized samples, *Appl. Opt.* **32**, 2976 (1993).
- [S3] D. B. Tanner, Use of x-ray scattering functions in Kramers-Kronig analysis of reflectance, *Phys. Rev. B* **91**, 035123 (2015).
- [S4] P. Blaha, K. Schwarz, G. Madsen, D. Kvasnicka, J. Luitz, R. Laskowski, F. Tran, and L. Marks, WIEN2k, An Augmented Plane Wave + Local Orbitals Program for Calculating Crystal Properties (Karlheinz Schwarz, Techn. Universität Wien, Austria), 2018. ISBN 3-9501031-1-2.
- [S5] P. Blaha, K. Schwarz, F. Tran, R. Laskowski, G. K. H. Madsen, and L. D. Marks, WIEN2k: An APW+lo program for calculating the properties of solids, *J. Chem. Phys.* **152**, 074101 (2020).
- [S6] J. P. Perdew, K. Burke, and M. Ernzerhof, Generalized Gradient Approximation Made Simple, *Phys. Rev. Lett.* **77**, 3865 (1996).
- [S7] X. Teng, L. Chen, F. Ye, E. Rosenberg, Z. Liu, J.-X. Yin, Y.-X. Jiang, J. S. Oh, M. Z. Hasan, K. J. Neubauer, B. Gao, Y. Xie, M. Hashimoto, D. Lu, C. Jozwiak, A. Bostwick, E. Rotenberg, R. J. Birgeneau, J.-H. Chu, M. Yi, and P. Dai, Discovery of charge density wave in a kagome lattice antiferromagnet, *Nature* **609**, 490 (2022).
- [S8] S. Shao, J.-X. Yin, I. Belopolski, J.-Y. You, T. Hou, H. Chen, Y. Jiang, M. S. Hossain, M. Yahyavi, C.-H. Hsu, Y. P. Feng, A. Bansil, M. Z. Hasan, and G. Chang, Intertwining of Magnetism and Charge Ordering in Kagome FeGe, *ACS Nano* **17**, 10164 (2023).
- [S9] G. Kresse and J. Furthmüller, Efficient iterative schemes for ab initio total-energy calculations using a plane-wave basis set, *Phys. Rev. B* **54**, 11169 (1996).
- [S10] C. Ambrosch-Draxl and J. O. Sofo, Linear optical properties of solids within the full-potential linearized augmented planewave method, *Comput. Phys. Commun.* **175**, 1 (2006).
- [S11] S. Fratini, S. Ciuchi, and D. Mayou, Phenomenological model for charge dynamics and optical response of disordered systems: Application to organic semiconductors, *Phys. Rev. B* **89**, 235201 (2014).
- [S12] U. Fano, Effects of Configuration Interaction on Intensities and Phase Shifts, *Phys. Rev.* **124**, 1866 (1961).
- [S13] A. Biswas, O. Iakutkina, Q. Wang, H. C. Lei, M. Dressel, and E. Uykur, Spin-Reorientation-Induced Band Gap in Fe₃Sn₂: Optical Signatures of Weyl Nodes, *Phys. Rev. Lett.* **125**, 076403 (2020).
- [S14] M. Wenzel, A. A. Tsirlin, O. Iakutkina, Q. Yin, H. C. Lei, M. Dressel, and E. Uykur, Effect of magnetism and phonons on localized carriers in the ferrimagnetic kagome metals GdMn₆Sn₆ and TbMn₆Sn₆, *Phys. Rev. B* **106**, L241108 (2022).
- [S15] E. Uykur, B. R. Ortiz, S. D. Wilson, M. Dressel, and A. A. Tsirlin, Optical detection of the density-wave instability in the kagome metal KV₃Sb₅, *npj Quantum Mater.* **7**, 16 (2022).
- [S16] H. Rammal, A. Ralko, S. Ciuchi, and S. Fratini, Transient localization from the interaction with quantum bosons (2023), [arXiv:2312.03840](https://arxiv.org/abs/2312.03840).
- [S17] M. Wenzel, A. A. Tsirlin, F. Capitani, Y. T. Chan, B. R. Ortiz, S. D. Wilson, M. Dressel, and E. Uykur, Pressure evolution of electron dynamics in the superconducting kagome metal CsV₃Sb₅, *npj Quantum Mater.* **8**, 45 (2023).
- [S18] M. Wenzel, B. R. Ortiz, S. D. Wilson, M. Dressel, A. A. Tsirlin, and E. Uykur, Optical study of RbV₃Sb₅: Multiple density-wave gaps and phonon anomalies, *Phys. Rev. B* **105**, 245123 (2022).
- [S19] M. Kawamura, FermiSurfer: Fermi-surface viewer providing multiple representation schemes, *Comput. Phys. Commun.* **239**, 197 (2019).
- [S20] B. R. Ortiz, S. M. L. Teicher, L. Kautzsch, P. M. Sarte, N. Ratcliff, J. Harter, J. P. C. Ruff, R. Seshadri, and S. D. Wilson, Fermi Surface Mapping and the Nature of Charge-Density-Wave Order in the Kagome Superconductor CsV₃Sb₅, *Phys. Rev. X* **11**, 041030 (2021).
- [S21] E. Uykur, B. R. Ortiz, O. Iakutkina, M. Wenzel, S. D. Wilson, M. Dressel, and A. A. Tsirlin, Low-energy optical properties of the nonmagnetic kagome metal CsV₃Sb₅, *Phys. Rev. B* **104**, 045130 (2021).
- [S22] M. Dressel and G. Grüner, *Electrodynamics of Solids: Optical Properties of Electrons in Matter* (Cambridge University Press, 2002).
- [S23] T. Hu, H. Pi, S. Xu, L. Yue, Q. Wu, Q. Liu, S. Zhang, R. Li, X. Zhou, J. Yuan, D. Wu, T. Dong, H. Weng, and N. Wang, Optical spectroscopy and band structure calculations of the structural phase transition in the vanadium-based kagome metal ScV₆Sn₆, *Phys. Rev. B* **107**, 165119 (2023).
- [S24] Y. Shao, A. N. Rudenko, J. Hu, Z. Sun, Y. Zhu, S. Moon, A. Millis, S. Yuan, A. I. Lichtenstein, D. Smirnov, Z. Q. Mao, M. I. Katsnelson, and D. N. Basov, Electronic correlations in nodal-line semimetals, *Nat. Phys.* **16**, 636 (2020).